

# Magnetic structure of $R_2\text{CoGa}_8$ ( $R = \text{Gd, Tb, and Dy}$ ): Structural tuning of magnetic properties in layered Ga-based intermetallic compounds

J. R. L. Mardegan, C. Adriano, R. F. C. Vescovi, G. A. Faria, P. G. Pagliuso, and C. Giles\*  
*Instituto de Física “Gleb Wataghin,” Universidade Estadual de Campinas, Campinas, São Paulo 13083-859, Brazil*  
 (Received 8 April 2013; revised manuscript received 27 January 2014; published 4 March 2014)

In this work we have determined the magnetic structure of  $R_2\text{CoGa}_8$  ( $R = \text{Gd, Tb, and Dy}$ ) intermetallic compounds using x-ray resonant magnetic scattering in order to study the evolution of the anisotropic magnetic properties along the series for  $R = \text{Gd-Tm}$ . The three compounds have a commensurate antiferromagnetic spin structure with a magnetic propagation vector  $\vec{\tau} = (\frac{1}{2}, \frac{1}{2}, \frac{1}{2})$  and a Néel temperature of approximately 20, 28.5, and 15.2 K for  $R = \text{Gd, Tb, and Dy}$ , respectively. The critical exponent  $\beta$  obtained from the temperature dependence of the magnetic peaks suggest a three-dimensional universality class for the three compounds. Comparing the simulated and integrated intensities we conclude that the magnetic moment direction is in the  $ab$  plane for the  $\text{Gd}_2\text{CoGa}_8$  compound and parallel to the  $c$  axis for the  $\text{Tb}_2\text{CoGa}_8$  and  $\text{Dy}_2\text{CoGa}_8$  compounds. The evolution of the magnetic properties of the  $R_2\text{CoGa}_8$  series for  $R = \text{Gd-Tm}$  is discussed taking into account the indirect Ruderman-Kittel-Kasuya-Yoshida interaction and crystalline-electric field effects. The comparison between the reported magnetic properties of the Ga-based compounds with those for the In-based isostructural family reveals differences in their exchange couplings that contribute to the understanding of the role of the  $f$ -electron magnetism in these classes of materials.

DOI: 10.1103/PhysRevB.89.115103

PACS number(s): 71.20.Lp, 75.25.-j, 75.50.Ee

## I. INTRODUCTION

The study of microscopic magnetic properties of intermetallic compounds in a given iso-structural series is an elucidating method to unravel the fundamental properties at work in complex materials. This is the case for the layered family  $R_nM_mX_{3n+2m}$  ( $R = \text{rare earth or actinides}$ ;  $M = \text{Co, Rh, Ir}$ ;  $X = \text{Ga or In}$ ;  $n = 1, 2$  and  $m = 0, 1$ ) with compounds that have exotic tunable ground states varying from antiferromagnetic (AFM) to superconductor (SC) or non-Fermi liquid behavior, among others [1–6]. As the superconductivity in these compounds is believed to be magnetically mediated, the systematic investigation along the series of intermetallic  $f$ -electron systems has usually been done by following the microscopic role of the Ruderman-Kittel-Kasuya-Yosida (RKKY) magnetic interaction and its relation with the crystalline electrical field (CEF) effects and crystal structures. In particular the magnetic structure determination is a very important step for the understanding of the physical properties since the magnetic moment direction, for example, carry information about the magnetic anisotropies created by the interaction between the  $f$  electrons and the surrounded conduction electrons and ions.

The  $R_nM_mX_{3n+2m}$  compounds with  $m = 1$  and  $n = 1$  or 2 are the crystallographic tetragonal variants of the cubic  $RX_3$  ( $m = 0, n = 1$ ). When a layer of  $MX_2$  is inserted along the  $c$  axis the  $RMX_5$  ( $m = 1, n = 1$ ) structure results (the so-called 115's). When an extra layer of  $RX_3$  is inserted the  $R_2MX_8$  ( $m = 1, n = 2$ ) structure is obtained (the so-called 218's) [6]. Some recent theoretical [7] and experimental [8–14] studies showed that the magnetic properties for all non-Kondo compounds of the family  $R_nM\text{In}_{3n+2}$  ( $n = 1, 2$ )

are mainly determined by the interplay between CEF effects and the RKKY interaction.

The particular interest of this work is to study the evolution of the anisotropic magnetic properties of the 218's Ga-based intermetallic compounds and to discuss this in a more general scenario where we compare the results with the trend found for the isostructural In-based compounds. In this regard, we have determined the magnetic structure of three members of the  $R_2\text{CoGa}_8$  ( $R = \text{Gd, Tb, Dy}$ ) series using the x-ray magnetic scattering (XRMS) technique. This study completes the determination of the magnetic structures of the synthesized compounds of the  $R_2\text{CoGa}_8$  series since the other members of this series have had its magnetic structure determined such as the  $\text{Ho}_2\text{CoGa}_8$  that was investigated by XRMS and neutron diffraction [14, 15] and  $\text{Er}_2\text{CoGa}_8$  and  $\text{Tm}_2\text{CoGa}_8$  investigated by powder neutron diffraction [16].

The intermetallic materials  $R_2\text{CoGa}_8$  ( $R = \text{Gd, Tb, and Dy}$ ) present a commensurate antiferromagnetic ordering with a magnetic propagation vector  $(\frac{1}{2}, \frac{1}{2}, \frac{1}{2})$ . For the  $R = \text{Tb and Dy}$  compounds, the direction of the magnetic moment was found parallel to the  $c$  axis and for the  $R = \text{Gd}$  the magnetic moment was found in the  $ab$  plane. These results allowed us to point out the differences in the magnetic structure of the Ga-based to the In-based compounds. Discussions based on the spin-only compounds ( $R = \text{Gd}$ ) are presented first and the role of crystalline-electric field effects are discussed next leading to a clear picture on the evolution of the anisotropic magnetic properties of the heavy rare earth Ga-based compounds along the  $R_2\text{CoGa}_8$  series.

## II. EXPERIMENTAL DETAILS

Single crystals of  $R_2\text{CoGa}_8$  were grown by the Ga-flux method as reported previously [3, 17]. The compounds have a tetragonal  $\text{Ho}_2\text{CoGa}_8$ -type structure (Space Group P4/mmm, No. 123). The phase and unit cell parameters were confirmed

\*Temporary address: Advanced Photon Source, Argonne National Laboratory, Argonne, Illinois 60439, USA; giles@ifm.unicamp.br

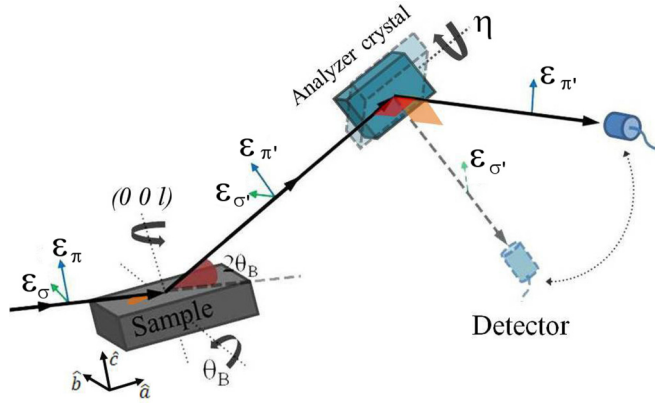


FIG. 1. (Color online) Experimental setup used in the XRMS measurements with polarization analysis. The crystals were mounted with the  $a$  axis of the sample initially aligned in the same direction as the incoming beam and with the  $(00l)$  reflections parallel to the azimuthal rotation axis  $\phi$ . Specular and off-specular peaks are accessible using a four-crystal geometry of the diffractometer.

by x-ray powder diffraction and are in good agreement with previous works [18]. The samples were cut and polished in order to have a flat surface perpendicular to the  $[001]$  direction with typical dimensions of approximately  $3 \times 2 \times 1 \text{ mm}^3$ .

The XRMS measurements were performed at the XRD2 beamline [19] of the Brazilian Synchrotron Light Laboratory (LNLS) in Campinas, Brazil. The energy of the incident beam was tuned to the  $L_2$  or  $L_3$  absorption edges of the rare earth element to enhance the magnetic signal. The crystals were cooled in a closed cycle He cryostat with Be domes and a Joule-Thomson cooling stage to achieve base temperature at 2 K. The samples were measured in the vertical diffraction plane and mounted in a four-circle diffractometer with its  $a$  axis initially aligned parallel to the incoming beam. Figure 1 illustrates the experimental setup used to perform the polarization analysis in our experiments where  $\theta_B$  is the Bragg angle, and  $\sigma$  and  $\pi$  ( $\sigma'$  and  $\pi'$ ) represent the components of the polarization of the incident (scattered) beam, respectively, perpendicular and parallel to the diffraction plane. The charge and magnetic scattering act differently on the polarization state of the diffracted beam, while the first does not mix the polarization components, the magnetic scattering (resonant or nonresonant) affects the polarization state. To detect the changes at different polarization channels a polarization analyzer was installed on the  $2\theta$  arm of the diffractometer allowing one to select, by a rotation of the angle  $\eta$  (Fig. 1), the two possible polarization channels for an incident beam that is  $\sigma$  polarized:  $\sigma - \sigma'$  and  $\sigma - \pi'$ . Due to the strong fluorescence of the Co-K edge at 7709 eV that lies very close to the Dy- $L_3$  resonant energy (7790 eV), the magnetic scattering data of the  $\text{Dy}_2\text{CoGa}_8$  was measured at the Dy- $L_2$  absorption edge (8581 eV) and we used a Cu(222) analyzer crystal. Measurements for the  $\text{Gd}_2\text{CoGa}_8$  and  $\text{Tb}_2\text{CoGa}_8$  compounds were performed at energies that matched closer to the Brewster angle of our pyrolytic-graphite analyzer crystal C(006), the Gd  $L_2$  edge at 7930 eV, and the Tb  $L_3$  edge at 7514 eV.

In addition, temperature dependence of the magnetic susceptibility measurements were performed in a commercial

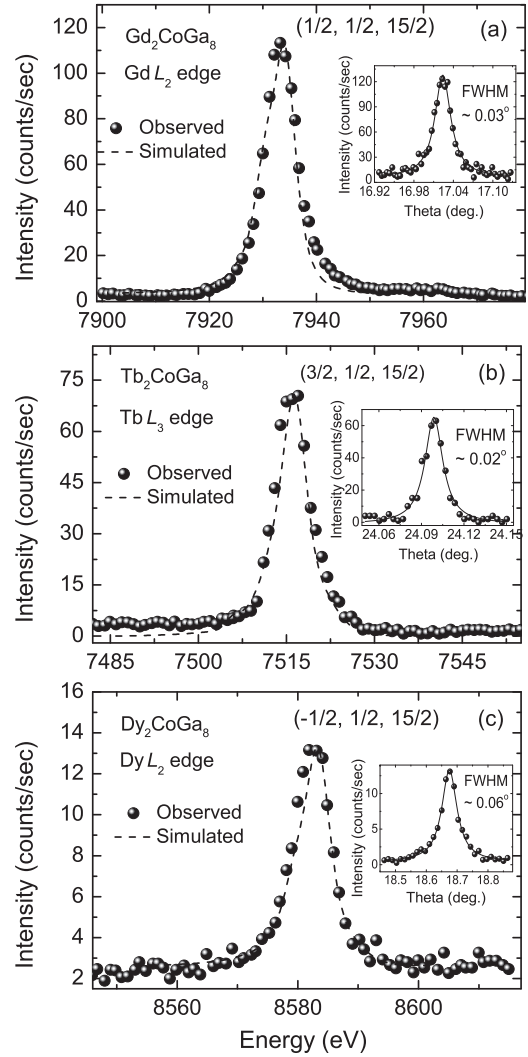


FIG. 2. Energy dependence of the resonant x-ray scattering signal in the  $\sigma - \pi'$  polarization channel of the  $R_2\text{CoGa}_8$  series for (a)  $R = \text{Gd}$ , (b)  $R = \text{Tb}$ , and (c)  $R = \text{Dy}$ . The dashed lines represent the simulated resonances using the FDMNES code corresponding to a pure electric dipolar transition ( $2p \rightarrow 5d$ ). The insets show the rocking curves of the magnetic Bragg peaks at the maximum enhancement energy and the calculated FWHM values were obtained by fitting the data with a pseudo-Voigt function.

superconducting quantum interference device (MPMS-SQUID) using a magnetic field of  $H = 0.1 \text{ T}$  applied parallel ( $\chi_{\parallel}$ ), and perpendicular ( $\chi_{\perp}$ ) to the  $c$  axis. Specific heat as a function of the temperature was also measured (not shown) in a commercial physical properties measurement system (PPMS) to better determine the AFM transition temperature of the samples.

### III. EXPERIMENTAL RESULTS

A systematic search in reciprocal space for magnetic Bragg peaks below the Néel temperature and with a polarization analyzer set to the  $\sigma - \pi'$  polarization channel revealed that the magnetic propagation vector is the  $(\frac{1}{2}, \frac{1}{2}, \frac{1}{2})$  for the three compounds. A search for other propagation vectors was

TABLE I. Parameters observed with XRMS for the  $R_2\text{CoGa}_8$  series ( $R = \text{Gd-Dy}$ ). The energy at the maximum resonance ( $E_{\text{max}}$ ), the FWHM of the energy line shape ( $w$ ), the peak intensity, and FWHM of the rocking curve ( $I_{\text{max}}$  and  $w'$ ), the resonant enhancement ( $\Delta$ ), the critical exponent ( $\beta$ ), and the Néel temperature ( $T_N$ ).

$R_2\text{CoGa}_8$							
R	$E_{\text{max}}$ (keV)	$w$ (eV)	$I_{\text{max}}$ (cps)	$w'$ (deg.)	$\Delta$	$\beta$	$T_N$ (K)
Gd	7.933	6.2	120	0.03	24	$0.32 \pm 0.09$	$20.0 \pm 0.5$
Tb	7.517	6.2	60	0.02	23	$0.36 \pm 0.03$	$28.5 \pm 0.5$
Dy	8.583	6.7	14	0.06	12	$0.36 \pm 0.07$	$15.2 \pm 0.5$

made but due to the limitation of XRMS in exploring the reciprocal space we cannot rule out completely its existence. Neutron scattering is the probe of choice for magnetic structure determination but in the case of Gd compounds it cannot be used due to the strong absorption cross section of Gd. The other compounds could have been measured with neutrons but due to the prompt availability of synchrotron sources their magnetic structure was investigated by XRMS only. The magnetic origin of these peaks was verified by probing its resonant energy line shape, its temperature dependence (vanishing above  $T_N$ ), and its polarization state (Stokes analysis) [20] showing that the polarization state of the diffracted beam followed the expected dipolar resonant scattering polarization dependence [21].

### A. Energy resonant line shapes

Typical resonant enhancements of the magnetic integrated intensity measured in the  $\sigma - \pi'$  polarization channel at the magnetic Bragg peaks  $(\frac{1}{2}, \frac{1}{2}, \frac{15}{2})$ ,  $(\frac{3}{2}, \frac{1}{2}, \frac{15}{2})$ , and  $(-\frac{1}{2}, \frac{1}{2}, \frac{15}{2})$  for  $\text{Gd}_2\text{CoGa}_8$ ,  $\text{Tb}_2\text{CoGa}_8$ , and  $\text{Dy}_2\text{CoGa}_8$ , respectively, are shown in Fig. 2.

These spectra were collected at 14 K for the Gd-based compound and at 2 K for the Tb- and Dy-based compounds. The maximum of these enhancements occurs 2–3 eV above the Gd- $L_2$ , Tb- $L_3$ , and Dy- $L_2$  absorption edges (Fig. 2) and show a single narrow resonant line shape typical of a pure dipolar transition (Table I). To test this hypothesis we performed first principle calculations using the FDMNES code [22] demonstrating that the resonant magnetic signal comes only from the dipolar transition ( $2p \rightarrow 5d$ ) as shown by the good fit of the pure electric dipolar simulated contribution (dashed line) to the experimental data in Fig. 2. The resonant enhancement extracted from the energy line shapes, shown in Table I, are of the same order of magnitude than the resonant enhancements expected for the pure metallic rare earth compounds [23] and at least two orders of magnitude less intense than the resonant enhancement found for its equivalent In-based compounds [13]. The peak intensity (in the  $\sigma - \pi'$  polarization channel) and the full width at half maximum (FWHM) of the magnetic rocking curves for the three compounds (insets of Fig. 2) are summarized in Table I. The  $\sigma - \sigma'$  components of the magnetic peaks (not shown) are all equal to zero.

### B. Magnetic order parameter

The temperature dependence of the magnetic reflections  $(\frac{1}{2}, \frac{1}{2}, \frac{15}{2})$ ,  $(\frac{3}{2}, \frac{1}{2}, \frac{15}{2})$ , and  $(-\frac{1}{2}, \frac{1}{2}, \frac{15}{2})$  for  $\text{Gd}_2\text{CoGa}_8$ ,  $\text{Tb}_2\text{CoGa}_8$ ,

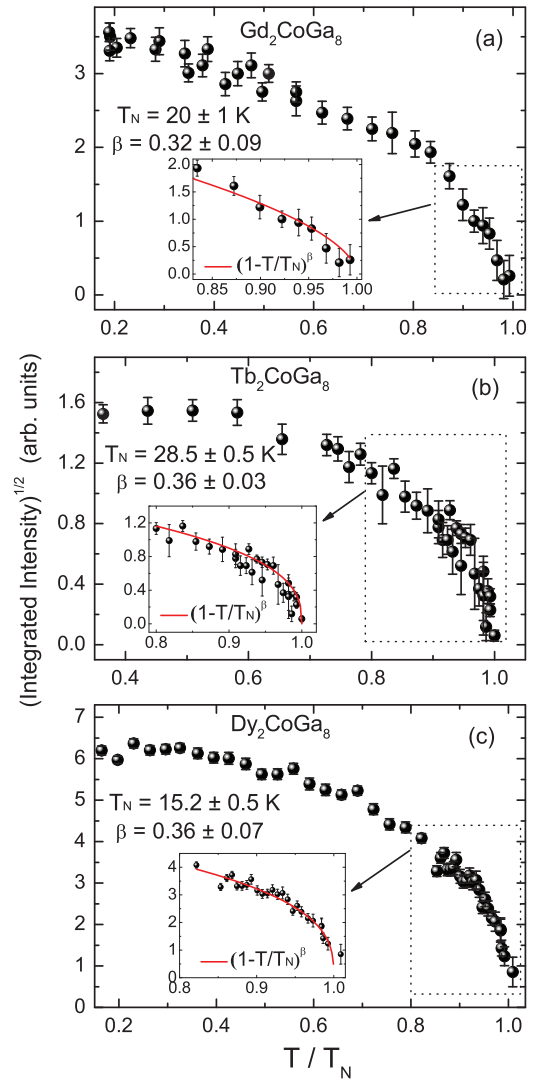


FIG. 3. (Color online) Temperature dependence of the squared root of the integrated intensity measured at the more intense magnetic Bragg peaks for the three compounds. (a) Magnetic Bragg peak  $(\frac{1}{2}, \frac{1}{2}, \frac{15}{2})$ , (b)  $(\frac{3}{2}, \frac{1}{2}, \frac{15}{2})$ , and (c)  $(-\frac{1}{2}, \frac{1}{2}, \frac{15}{2})$  for the  $\text{Gd}_2\text{CoGa}_8$ ,  $\text{Tb}_2\text{CoGa}_8$ , and  $\text{Dy}_2\text{CoGa}_8$  compounds, respectively. The insets show the  $T_N$  and the critical exponent  $\beta$  obtained using a critical power-law expression,  $(1 - T/T_N)^\beta$ .

and  $\text{Dy}_2\text{CoGa}_8$ , respectively, are shown in Fig. 3. The square root of the integrated intensity of the magnetic peaks decreases continuously as the temperature approaches the Néel temperature typical of a second-order phase transition. The insets in Fig. 3 show a fitting using a critical power-law expression,  $(1 - T/T_N)^\beta$ , near the phase transition. From the fitting we can extract  $T_N$  and the critical exponent  $\beta$  for each compound. The  $T_N$  found by x-ray diffraction are shown in Table I and are in good agreement with the  $T_N$  obtained by our macroscopic measurements (see Table II). The critical exponent  $\beta$  found for the three compounds suggest a three-dimensional (3D) magnetic model [24]. Nevertheless we cannot distinguish between a 3D-Ising, X-Y, or Heisenberg model.

### C. Magnetic structure determination

To determine the magnetic structure of the  $R_2\text{CoGa}_8$  compounds we first used the program *SARAh*-Representational Analysis [25] to calculate the possible magnetic configurations. For the magnetic wave vector  $(\frac{1}{2}, \frac{1}{2}, \frac{1}{2})$  and the  $P4/mmm$  space group, the magnetic representation ( $\Gamma_{\text{Mag}}$ ) can be decomposed in eight one-dimensional ( $1\text{D}-\Gamma_{1-8}^1$ ) and two two-dimensional ( $2\text{D}-\Gamma_{9,10}^2$ ) irreducible representations (IR's). Nevertheless only four of these 10 representations (two  $1\text{D}-\Gamma_{2,3}^1$  and two  $2\text{D}-\Gamma_{9,10}^2$ ) enter into the global reducible magnetic representation on the  $2g$  Wyckoff crystallographic position (coordinates,  $0,0,z$ ) occupied by the rare earth ion and compatible with the fact that the Co and Ga ions do not carry magnetism in these compounds. Therefore the magnetic representation (MR) can be written as

$$\Gamma_{\text{Mag}} = \Gamma_2^1 + \Gamma_3^1 + \Gamma_9^2 + \Gamma_{10}^2. \quad (1)$$

Details about the IR's are described in Appendix A. Using these magnetic configurations we could determine the direction of the magnetic moments for the  $R_2\text{CoGa}_8$  compounds by comparing simulated intensities with the experimental integrated intensities.

The simulated intensities were calculated using a dipolar resonant x-ray magnetic scattering cross section [9,21,26,27] model given by

$$I \propto A * LF * \left| \sum_n f_n(\vec{k}, \hat{\epsilon}, \vec{k}', \hat{\epsilon}', \hat{z}_n) e^{i\vec{Q} \cdot \vec{R}_n} \right|^2, \quad (2)$$

where  $A = \frac{\sin(\theta+\alpha)\sin(\theta-\alpha)}{\sin\theta\cos\alpha}$  is the absorption correction for off-specular reflections with Bragg angle  $\theta$  and asymmetry angle  $\alpha$  (defined as the angle between the reciprocal lattice vector  $\vec{Q}$  and the normal to the surface of the crystal, here parallel to the  $c$  direction),  $LF = \frac{1}{\sin(2\theta)}$  is the Lorentz factor, and the term inside the absolute square is the magnetic structure factor. The term  $f_n$  is the resonant magnetic scattering amplitude, and  $\vec{k}$  ( $\hat{\epsilon}$ ) and  $\vec{k}'$  ( $\hat{\epsilon}'$ ) are the incident and scattered wave (polarization) vectors, respectively.  $\vec{R}_n$  is the position of the  $n$ th atom in the unit cell, and  $\hat{z}_n$  is the moment direction at the  $n$ th site. Solving the absolute square in Eq. (2) for the reflections of the type

TABLE II. Parameters obtained from XRMS, neutron, and macroscopic measurements for the  $R_2\text{CoGa}_8$  series ( $R = \text{Gd-Tm}$ ). The Néel temperature ( $T_N$ ), the magnetic propagation vector ( $\vec{\tau}$ ), the AFM coupling along  $c$  axis (Model), and the direction of magnetic moment ( $\hat{z}_n$ ) were obtained by neutron and x-ray diffraction.<sup>a</sup> The effective magnetic moment ( $\mu_{\text{eff}}$ ), the paramagnetic Curie-Weiss temperature ( $\theta_{\text{CW}}$ ), and the Néel temperature ( $T_{N,Cp}$ ) were obtained by our macroscopic measurements and the CEF parameters ( $B_2^0$ ,  $\mathcal{J}_{\text{ex}}^c/k_B$ , and  $\mathcal{J}_{\text{ex}}^{ab}/k_B$ ) were extracted from Ref. [18].

$R_2\text{CoGa}_8$										
$R$	$T_N$ (K)	$T_{N,Cp}$ (K)	$\mu_{\text{eff}}$ ( $\mu_B$ )	$\theta_{\text{CW}}$ (K)	$\vec{\tau}$	Model	$\hat{z}_n$	$B_2^0$ (K)	$\mathcal{J}_{\text{ex}}^c/k_B$ (K)	$\mathcal{J}_{\text{ex}}^{ab}/k_B$ (K)
Gd	$20.0 \pm 0.5$	$19.4 \pm 0.5$	$7.3 \pm 0.5$	$-28 \pm 3$	$(\frac{1}{2}, \frac{1}{2}, \frac{1}{2})$	(+ + - -)	$\perp \hat{c}$	—	—	—
Tb	$28.5 \pm 0.5$	$29.5 \pm 0.5$	$9.6 \pm 0.5$	$-35 \pm 2$	$(\frac{1}{2}, \frac{1}{2}, \frac{1}{2})$	(+ + - -)	$\parallel \hat{c}$	-1.61	-4.94	-2.24
Dy	$15.2 \pm 0.5$	$15.8 \pm 0.5$	$10.5 \pm 0.5$	$-16 \pm 2$	$(\frac{1}{2}, \frac{1}{2}, \frac{1}{2})$	(+ + - -)	$\parallel \hat{c}$	-0.7	-1.94	-1.28
Ho	$5.1 \pm 0.5$	$5.1 \pm 0.5$	$10.3 \pm 0.5$	$-11 \pm 1$	$(\frac{1}{2}, \frac{1}{2}, \frac{1}{2})$	(+ + - -)	$\parallel \hat{c}$	-0.22	-0.59	-0.51
Er	$3.0 \pm 0.5$	$2.9 \pm 0.5$	$9.3 \pm 0.5$	$-7 \pm 1$	$(0, \frac{1}{2}, 0)$	(+ - + -)	$\perp \hat{c}$	0.089	-0.32	-0.35
Tm	$2.0 \pm 0.5$	$2.1 \pm 0.5$	$8.1 \pm 0.5$	$-6 \pm 1$	$(\frac{1}{2}, 0, \frac{1}{2})$	(+ + - -)	$\perp \hat{c}$	0.35	-0.075	-0.53

<sup>a</sup>The data for  $R = \text{Ho}$  are from Refs. [14] and [15] and for  $R = \text{Er}$  and  $\text{Tm}$  are from Ref. [16].

$(\frac{1}{2}, \frac{1}{2}, \frac{L}{2})$ , the magnetic intensity is proportional to  $\sin^2(\theta + \alpha) * B$  or  $\cos^2(\theta + \alpha) * B$ , for the moments aligned parallel ( $\Gamma_2$  or  $\Gamma_3$ ) or perpendicular ( $\Gamma_9$  or  $\Gamma_{10}$ ) to the  $c$  direction, respectively. The  $B$  term depends on the coupling between the rare earths ions and it can be written as  $\sin^2(2\pi LR_n)$  for the model I and  $\cos^2(2\pi LR_n)$  for the model II (see details in Appendix A).

Figure 4 shows the normalized integrated intensities of the experimental magnetic reflections and the simulated magnetic peaks as a function of  $L$  for  $\text{Gd}_2\text{CoGa}_8$  [Fig. 4(a)],  $\text{Tb}_2\text{CoGa}_8$  [Fig. 4(b)], and  $\text{Dy}_2\text{CoGa}_8$  [Fig. 4(c)] compounds. For each compound, five off-specular magnetic reflections (belonging to the same crystallographic zone) were measured and the normalized integrated intensities are shown in Fig. 4 as symbols. Other magnetic Bragg peaks were measured (not shown) but due to the difficulty to correct the absorption intensity, we only used the magnetic reflections belonging to the same crystallographic zone (and having the same absorption correction) shown in Fig. 4. The calculated intensities were obtained using Eq. (2) for four different MRs ( $\Gamma_2$ ,  $\Gamma_3$ ,  $\Gamma_9$ , and  $\Gamma_{10}$ ).

Comparing the simulated intensities and the experimental data normalized to the peaks with  $L = \frac{15}{2}$  we can determine the direction of magnetic moment for the three compounds. Figure 4(a) shows that the magnetic Gd moments are arranged according to the IR  $\Gamma_{10}$ , i.e., the magnetic moments perpendicular to the  $c$  axis with a coupling (+ + - -). On the other hand, Figs. 4(b) and 4(c) indicate that the magnetic Tb and Dy moments are arranged according to the IR  $\Gamma_2$ , thus the magnetic moments are aligned parallel to the  $c$  axis with a coupling (+ + - -).

Figure 5 describes the final magnetic structure of  $\text{Gd}_2\text{CoGa}_8$  [Fig. 5(a)] and  $\text{Tb}_2\text{CoGa}_8$  and  $\text{Dy}_2\text{CoGa}_8$  [Fig. 5(b)] including the coupling of the rare-earth ions in the  $c$  axis and the magnetic moment direction.

### D. Macroscopic measurements

To complete the study of the evolution of the magnetic properties of the  $R_2\text{CoGa}_8$  series we have performed magnetic susceptibility and specific heat measurements for  $R = \text{Gd-Tm}$ . The later results (not shown) were used to extract the Néel

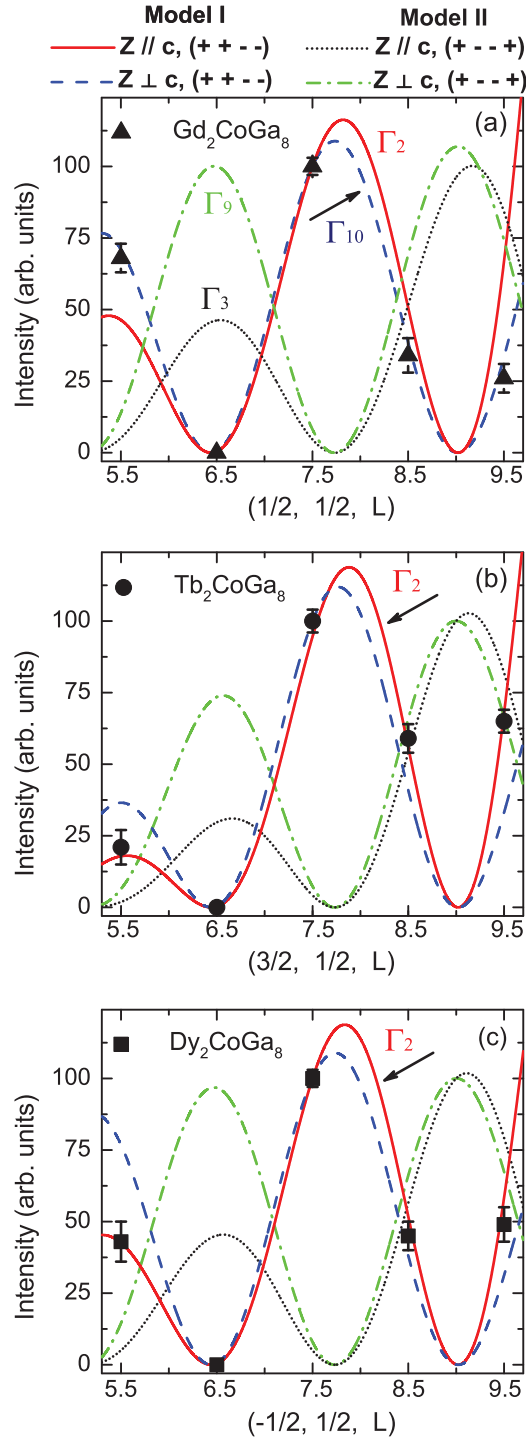


FIG. 4. (Color online) Normalized integrated intensities of the magnetic Bragg peaks for (a)  $\text{Gd}_2\text{CoGa}_8$ , (b)  $\text{Tb}_2\text{CoGa}_8$ , and (c)  $\text{Dy}_2\text{CoGa}_8$ . The experimental data are compared to the calculated intensities using Eq. (2). The simulated intensities were obtained considering four possible configurations ( $\Gamma_2$ ,  $\Gamma_3$ ,  $\Gamma_9$ , and  $\Gamma_{10}$ ): two possible magnetic couplings ( $++--$ ) and ( $+--+$ ), and two possible magnetic moment directions related to the to  $c$  direction ( $\hat{z}_n \parallel \hat{c}$  or  $\hat{z}_n \perp \hat{c}$ ). The arrow in each panel shows the best agreement between the experimental and simulated results.

temperature summarized in Table II as  $T_{N,Cp}$ . Figure 6 shows the temperature dependence of the magnetic susceptibility

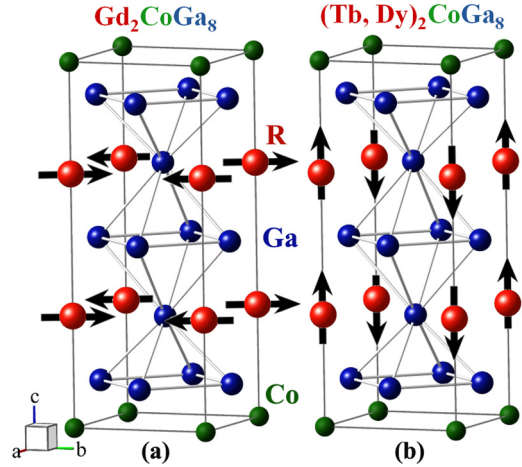


FIG. 5. (Color online) The magnetic structure of  $R_2\text{CoGa}_8$  ( $R = \text{Gd-Dy}$ ) compounds with propagation vector  $(\frac{1}{2}, \frac{1}{2}, \frac{1}{2})$  and with a ( $++--$ ) coupling of the rare earth ions in the  $c$  axis. Magnetic structure of the (a)  $\text{Gd}_2\text{CoGa}_8$  with the magnetic moments lying in the  $ab$  plane and (b)  $(\text{Tb, Dy})_2\text{CoGa}_8$  compounds with the magnetic moments aligned along the  $c$  direction.

for  $R_2\text{CoGa}_8$  ( $R = \text{Gd-Dy}$ ) measured with a magnetic field of  $H = 0.1$  T applied parallel ( $\chi_{\parallel}$ , closed symbols) and perpendicular ( $\chi_{\perp}$ , open symbols) to the  $c$  axis between 2 and 300 K. The insets in Fig. 6 show the susceptibility inverse of the polycrystalline average data taken as  $\chi_{\text{poly}} = (\chi_{\parallel} + 2\chi_{\perp})/3$  for the three compounds. Fits from the inverse of  $\chi_{\text{poly}}(T)$  for  $T > 150$  K performed for the  $R = \text{Gd-Tm}$  series using a Curie-Weiss law yielding the determination of the effective magnetic moment  $\mu_{\text{eff}}$  and the paramagnetic Curie-Weiss temperature  $\theta_{\text{CW}}$  for the compounds, are summarized in Table II. The effective magnetic moments are very close to the theoretical values expected for the rare-earth free ions [28]. The fits for  $R = \text{Gd, Tb, and Dy}$  are shown in red lines in the insets of Fig. 6.

It is important to notice from the susceptibility measurements that  $\text{Gd}_2\text{CoGa}_8$  presents the expected anisotropic behavior for an antiferromagnet for  $T < T_N$  with a magnetic-easy axis perpendicular to the  $c$  direction. The paramagnetic phase has no anisotropy in agreement with the fact that Gd has no orbital contribution ( $L = 0$ ) therefore no first-order CEF effects. On the other hand, Figs. 6(b) and 6(c) show for both  $(\text{Tb,Dy})_2\text{CoGa}_8$  compounds a magnetic easy axis along the  $c$  direction. The anisotropy of the susceptibility data in the paramagnetic phase is due to the strong CEF effects found in these compounds, as will be discussed later in Sec. IV B. All the above results corroborate with the magnetic structures determined in Section III C.

#### IV. DISCUSSIONS

The determination of the magnetic structures for the  $R_2\text{CoGa}_8$  compounds with  $R = \text{Gd-Dy}$  allow us to have a complete picture of the magnetic structures of the family of Ga-based compounds for  $R = \text{Gd-Tm}$ . The main results are summarized in Table II.

It is important to observe first the evolution of the Néel temperature, the propagation vector, and the magnetic coupling

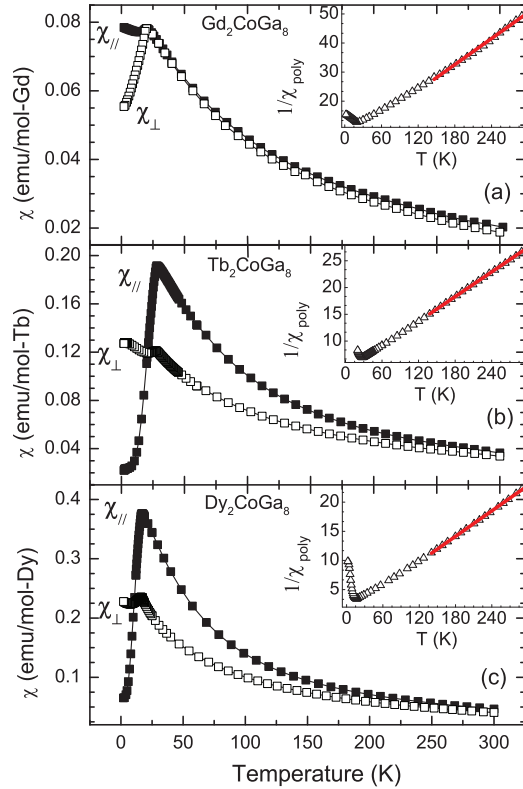


FIG. 6. (Color online) Magnetic susceptibility as a function of temperature measured with a magnetic field of  $H = 0.1$  T applied parallel ( $\chi_{\parallel}$ ) and perpendicular ( $\chi_{\perp}$ ) to the  $c$  axis for (a)  $\text{Gd}_2\text{CoGa}_8$ , (b)  $\text{Tb}_2\text{CoGa}_8$ , and (c)  $\text{Dy}_2\text{CoGa}_8$  compounds. The insets show the inverse magnetic susceptibility of the polycrystalline average data taken as  $\chi_{\text{poly}} = (\chi_{\parallel} + 2\chi_{\perp})/3$ .

of the rare earth atoms along the series. The Néel temperature of the Gd compound is 20 K, it increases to 28.5 K for the Tb compound and decreases to 15.2 K for the Dy compound, and drops below 5.1 K for all the other compounds, reaching 2 K for the Tm compound. The Néel temperatures of the  $R_2\text{CoGa}_8$  compounds are the lowest when compared to the In-based compounds with  $M = \text{Ir, Rh or Co}$  [10,18]. The propagation vector  $(\frac{1}{2}, \frac{1}{2}, \frac{1}{2})$  and the magnetic coupling along the  $c$  direction ( $++--$ ) are the same for the compounds with  $R = \text{Gd to Ho}$ , but do change for the  $R = \text{Er and Tm}$  compounds. In addition, the magnetic moment is aligned along the  $c$  direction for  $R = \text{Tb, Dy, and Ho}$  and perpendicular to the  $c$  direction for  $R = \text{Gd, Er, and Tm}$ . In the following we will discuss how the microscopic magnetic properties of the Ga-based compounds are the result of the interplay of the RKKY interaction and the CEF effects similar to the In-based compounds but with the important differences in their electronic and crystallographic properties due to the substitution of Ga ions with small radius and  $4p$  bands to the In ions with larger radius and  $5p$  bands.

#### A. RKKY interaction in the $\text{Gd}_2MX_8$ compounds

It is instructive to start comparing the magnetic structure and microscopic properties of the In-based and Ga-based  $\text{Gd}_2MX_8$  compounds ( $M = \text{Co, Rh, Ir}$  for  $X = \text{In}$ , and

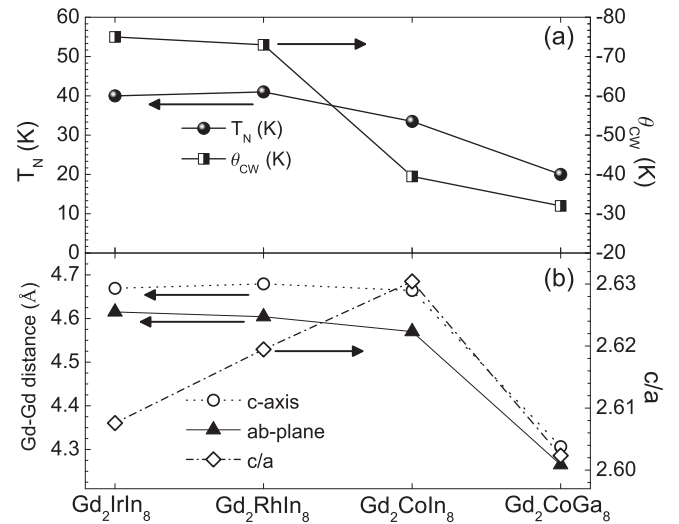


FIG. 7. (a) Shows the comparison between the Néel temperatures (solid circle symbols) and the Curie-Weiss theta (half-filled square symbols) of the  $\text{Gd}_2MX_8$ ,  $M = \text{Ir, Rh, Co}$  for  $X = \text{In}$ , and  $M = \text{Co}$  for  $X = \text{Ga}$  compounds. (b) Shows the first nearest neighbor distances in the  $c$  direction (open circle symbols) and in the  $ab$  plane (solid triangle symbols). We also present the  $c/a$  ratio (open diamond symbols) for these compounds. For completeness, the Gd-Gd distance for  $\text{GdIn}_3$  is 4.6068 Å [10].

$M = \text{Co}$  for  $X = \text{Ga}$ ). These are the spin-only compounds (with  $L = 0$ ) in this series, since the Gd ion has a half-filled  $4f$  shell being spherically symmetric and its magnetic properties are mainly determined by the RKKY interaction with no effects from the crystal-field anisotropy or spin-orbit coupling.

Figure 7(a) shows the evolution of the Néel temperature and the Curie-Weiss temperature (obtained from the high temperature  $T > 150$  K fits of the susceptibility data). Figure 7(b) describes the first and second nearest neighbor Gd-Gd distance and the  $c/a$  ratio for these four compounds. The Néel temperature for the  $\text{Gd}_2\text{IrIn}_8$  is 40 K very close to the one for the  $\text{Gd}_2\text{RhIn}_8$  compound ( $T_N = 41$  K) but decreases by almost 20% for the  $\text{Gd}_2\text{CoIn}_8$  ( $T_N = 33$  K) and by 50% for the  $\text{Gd}_2\text{CoGa}_8$  ( $T_N = 20.0$  K). This astonishing change of the Néel temperature in Gd compounds of the same crystallographic structure is here followed by a similar strong decrease of the Curie-Weiss temperature reflecting an effective decrease of the exchange interaction in the Ga-based compounds.

These observations indicate that the decrease of the exchange coupling  $J$  may be related to the substitution of In by Ga due to a possible reduced hybridization of the more localized Ga  $4p$  band against the broader In  $5p$  band. This scenario is supported by the small resonant enhancement of the XRMS signal at the  $L_2$  edges observed for the  $\text{Gd}_2\text{CoGa}_8$  (Table I) as compared to the reported three orders of magnitude resonant enhancement for the  $\text{Gd}_2\text{IrIn}_8$  compound [13]. The existence of a large XRMS enhancement at the  $L$  edge due to dipolar resonance ( $2p \rightarrow 5d$ ) indicates a high magnetic polarization of the Gd  $5d$  electronic levels due to hybridization with magnetic  $4f$  electrons. This effect can occur for Gd ions in neighboring sites via In  $5p$  levels for the  $\text{Gd}_2\text{IrIn}_8$ . The

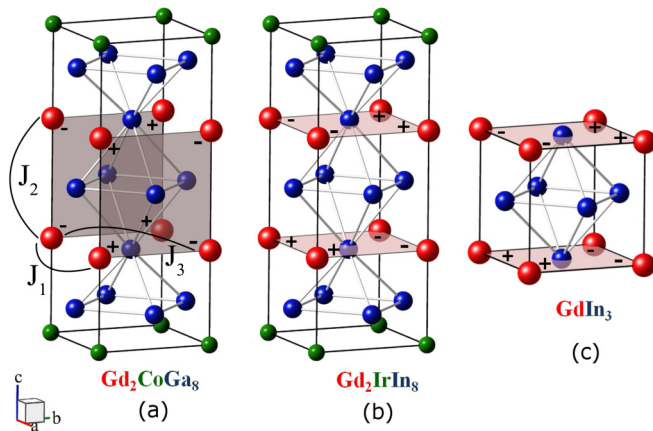


FIG. 8. (Color online) Comparison of the magnetic coupling found in the (a)  $\text{Gd}_2\text{CoGa}_8$ , (b)  $\text{Gd}_2\text{IrIn}_8$ , and (c)  $\text{GdIn}_3$ . The shaded plane indicates similar coupling schemes to highlight the differences between the Ga-based and In-based compounds. The exchange couplings for the first- ( $J_1$ ), the second- ( $J_2$ ), and third-nearest-neighbors ( $J_3$ ) for the (218) structure are also shown for clarity.

small XRMS enhancement in the  $\text{Gd}_2\text{CoGa}_8$  compound could then be a consequence of the reduced hybridization of the Gd  $5d-4f$  electronic levels via Ga  $4p$  levels.

Furthermore a direct comparison of the magnetic structure of the  $\text{Gd}_2\text{CoGa}_8$  compound to the only Gd-related compound with a known magnetic structure  $\text{Gd}_2\text{IrIn}_8$  shows important differences in their microscopic magnetic properties. The magnetic structure of the  $\text{Gd}_2\text{CoGa}_8$  found in this work corresponds to a C-AFM structure (in analogy to the description used for the cubic perovskites [28]) with an AFM coupling between the first nearest neighbors in the  $ab$  plane and an FM coupling in the  $c$  direction corresponding to the second nearest neighbors [Figs. 5(a) and 8(a)]. On the contrary, although the  $\text{Gd}_2\text{IrIn}_8$  compound [13] can be also viewed as a C-AFM structure the magnetic coupling is FM in one direction in the  $ab$  plane and AFM along the two other perpendicular directions, i.e., the FM coupling is not anymore along the  $c$  axis but is in the plane perpendicular to the  $c$  axis [Fig. 8(b)]. The magnetic coupling of these two compounds are compared to the  $\text{GdIn}_3$  magnetic structure [Fig. 8(c)] which possesses a C-AFM coupling. In the three compounds the magnetic moment is found lying in the  $ab$  plane.

In these compounds the magnetic coupling between the Gd ions originates from the RKKY mechanism, and their ground state is determined by the relative strength among the first- ( $J_1$ ), the second- ( $J_2$ ), and third-nearest-neighbors ( $J_3$ ) exchange couplings [Fig. 8(a)]. For the Gd compounds the magnetic coupling between rare earth ions is determined by anisotropic interactions which is mainly due to magnetic dipolar interactions due to the lack of crystal field effects. In this perspective the different magnetic couplings found in the Ga-based compounds (for  $R = \text{Gd}$ , and also for  $R = \text{Dy}$ ,  $\text{Tb}$ , and  $\text{Ho}$ ) as compared to the In-based compounds determine different exchange coupling relative strength ( $J_1/J_3$ ) and reveal interesting differences in the physical properties of these two families of intermetallic compounds.

Indeed, by using an estimate of the density of states for the  $\text{Gd}_2M\text{In}_8$  compounds of 1.4 states/eV per mol and per spin [29], we can estimate the magnitude of exchange couplings finding that the  $J_1$  ( $J_2$ ) favors an FM coupling along the first- (second-) nearest-neighbors Gd ions and  $J_3$  favors an AFM coupling along the third-nearest neighbors. This scenario explains well the magnetic coupling found for the  $\text{Gd}_2\text{IrIn}_8$  compound in the  $ab$  plane. The  $J_3$  coupling is satisfied and the  $J_1$  is partly satisfied leading to some kind of magnetic frustration that is minimized by the actual magnetic coupling of Gd ions in the  $ab$  plane. This magnetic coupling breaks the tetragonal symmetry of the crystallographic structure. The AFM magnetic coupling of the Gd ions along the  $c$  direction [Fig. 8(b)] (that according to the value of  $J_2$  should be FM and have the same coupling as the first-nearest neighbor in the  $ab$  plane), is a clear demonstration of the anisotropic electronic layered properties of these compounds. A direct confirmation on these properties could be revealed by angle-resolved photoemission spectroscopy measurements on the  $\text{Gd}_2M\text{In}_8$  compounds.

As such, the combination of the reduction of the first neighbor Gd-Gd distances for the Ga-based compounds compared to the In compounds and the decrease of the hybridization between the Ga  $p$  states with the  $f$  electrons with respect to the In  $p$  states can qualitatively explain the observed changes in the magnetic structures of these Gd compounds. These two effects combined are in fact responsible for the modifications in the relative coupling exchanges  $J_1/J_2$  and  $J_1/J_3$  between the Gd ions in the Ga and In-based series, leading to a more two-dimensional character (tetragonal) of the magnetic structure in the Ga-based compounds. This result may be useful to understand the difference between the nature of the  $f$ -electron spin fluctuations in the presumably magnetically mediated heavy-fermion superconductors in related Ga and In-based series.

## B. CEF effects in the $R_2\text{CoGa}_8$ structure

In a simplified mean-field model and in the absence of any crystal field effect it is expected that the evolution of the Néel temperature along the series of  $R_2\text{CoGa}_8$  with  $R = \text{Gd-Tm}$  would follow the de Gennes scaling  $(g_j - 1)^2 J(J + 1)$  where  $g_j$  is the Landé  $g$  factor and  $J$  is the total angular momentum. The actual evolution of Néel temperatures for this series is presented in Table II and Fig. 9 (squared symbols). It is clear that a very strong deviation from this scaling occurs for the  $R = \text{Tb}$  and  $\text{Dy}$ , increasing its transition temperatures, while the Néel temperature follow the de Gennes scaling for  $R = \text{Ho}$  to  $\text{Tm}$ . The deviation from this scaling is expected for the non-S rare earth ions of this series and can be ascribed to CEF effects [7] as we will discuss below. In the Ga-based compounds the effect is stronger for the  $\text{Tb}$  and  $\text{Dy}$  ions and this is a strong indication that the CEF effects are larger for the largest non-S ions,  $\text{Tb}$  and  $\text{Dy}$ , and have reduced effects for the heavier and smaller rare earths ions.

Furthermore we argue here that this effect is enhanced for the Ga-based compounds as compared to the In-based compounds.

Indeed in Fig. 9 we also show the de Gennes scaling for the  $R_2\text{RhIn}_8$  and  $R_2\text{CoIn}_8$  series of heavy rare earth compounds.

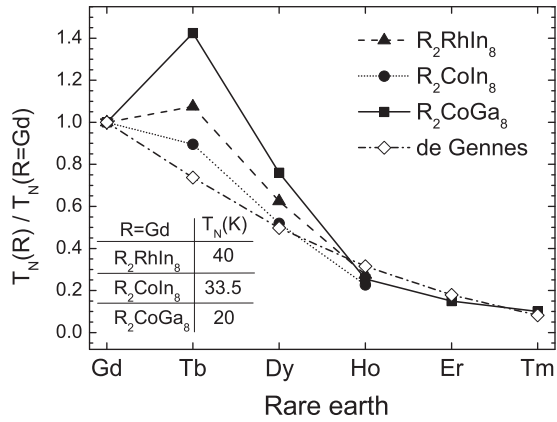


FIG. 9. Deviation of the Néel temperatures from the de Gennes scaling (diamond open symbols) for the series of compounds  $R_2CoGa_8$  with  $R = Gd$  to  $Tm$  (square symbols),  $R_2CoIn_8$  for  $R = Gd$  to  $Ho$  (circle symbols), and  $R_2RhIn_8$  for  $R = Gd$  to  $Ho$  (triangle symbols). The Néel temperatures are normalized by the Néel temperature of their corresponding  $R = Gd$  member of the series; these values are shown in the inset table of this figure. The dashed and continuous lines are just guides for the eye.

All the curves are presented as normalized curves by the  $R = Gd$  compound of its series (with the Néel temperatures for the respective  $R = Gd$  compound shown in the inset table of Fig. 9) to compare the relative deviation from the de Gennes scaling for these series. In particular we observe a more than 100% deviation of the de Gennes scaling for the  $Tb_2CoGa_8$  followed by 80% deviation for the  $Tb_2RhIn_8$  and 30% deviation for the  $Tb_2CoIn_8$ . The deviation of the Néel temperature from the de Gennes scaling is also present in the other series of  $R_2MIn_8$  and is always larger for the  $Tb$  and  $Dy$  compounds but is maximized in the  $R_2CoGa_8$  series. A crystalline electric field analysis for the  $R_2CoGa_8$  series has already been performed by Joshi *et al.* [18], by considering a CEF Hamiltonian for tetragonal symmetry and fitting the susceptibility data to a CEF model.

The CEF parameters determine the tendency of spins to order in-plane or out-of-plane and the dominant CEF parameter  $B_{20}$  is presented in Table II. We also present the exchange coupling along the [100] ( $\mathcal{J}_{ex}^{ab}$ ) and [001] ( $\mathcal{J}_{ex}^c$ ) obtained from a simplified relation between  $B_{20}$  and the paramagnetic Curie-Weiss temperature [18]. The negative value of  $B_{20}$  is in agreement with the observed ordering moment direction found for these compounds, i.e., aligned with the  $c$  axis. For the  $R = Er$  and  $Tm$  compounds the value of  $B_{20}$  becomes positive and this is also in agreement with the experimental observations [16] where the moment is aligned in the  $ab$  plane. The relative strength of the exchange couplings along the  $c$  axis ( $\mathcal{J}_{ex}^c$ ) or perpendicular to the  $c$  axis ( $\mathcal{J}_{ex}^{ab}$ ) and their sign suggests the correct coupling (antiferromagnetic) and moment direction for all the compounds in this series. For the  $Tb$  and  $Dy$  compounds  $\Delta\mathcal{J}_{ex} (= \mathcal{J}_{ex}^{ab} - \mathcal{J}_{ex}^c)$  is large and positive describing a strong magnetic anisotropy created by CEF effects and visible in the susceptibility data presented in Fig. 6. For the  $R = Ho$  compound  $\Delta\mathcal{J}_{ex}$  approaches zero but is still positive and then reverses its sign for the  $R = Er$  and  $Tm$  compounds, compatible with the moment

direction found in these compounds. It is interesting to note that the  $R = Ho$  compound is at a crossover region between different magnetic moment orientation and coupling. A detailed discussion on the physical properties of the  $R = Ho$  compounds is presented elsewhere, together with the magnetic structure determination by neutron diffraction [15]. It is worth noting here that in the absence of crystal field effects, as in the case of  $Gd_2CoGa_8$ , the magnetic moment lies in the  $ab$  plane.

## V. CONCLUSIONS

The systematic study of the magnetic properties of the  $R_2CoGa_8$  series of compounds for  $R = Gd$  to  $Tm$ , allowed us to point out important differences introduced by the substitution of  $In$  by  $Ga$  in these series. By analyzing the magnetic properties of the  $R = Gd$  compounds, we concluded that the substitution of  $In$  by  $Ga$  affects both the strength of the exchange coupling (observed by the reduced Néel temperature) and the symmetry of the magnetic coupling (observed by determining the magnetic structure of these compounds) and reveals a more two-dimensional structure in the  $Ga$ -based compound than in the  $In$ -based compound. The comparison of the non-S members of these series allowed us to conclude that the CEF effects are stronger in the  $Ga$ -based compounds as compared to the  $In$ -based compounds observed by the larger de Gennes deviation of the Néel temperature and the larger magnetic anisotropy quantified by  $\Delta\mathcal{J}_{ex}$ . Furthermore, we speculate that there may be an optimized dimension of the tetragonal unit cell that enhances the CEF effects, corresponding to the lattice parameters of the  $R = Tb$  and  $Dy$  compounds.

We believe that the differences in the magnetic properties of the  $Ga$ -based compounds to the  $In$ -based compounds pointed out in this work may add new ingredients to the understanding of the differences in the physical properties for the well-known

TABLE III. Basis vectors (BVs) for the space group  $P4/mmm$  with  $\mathbf{k}_{20} = (\frac{1}{2}, \frac{1}{2}, \frac{1}{2})$ . The rare earth atoms of the nonprimitive basis are defined according to 1 (0,0,z) and 2 (0,0,1-z), where  $z$  is the atomic position of rare earth within the unit cell.

IR	BV	Atom	BV components					
			$m_{\parallel a}$	$m_{\parallel b}$	$m_{\parallel c}$	$im_{\parallel a}$	$im_{\parallel b}$	$im_{\parallel c}$
$\Gamma_2$	$\psi_1$	1	0	0	1	0	0	0
		2	0	0	1	0	0	0
$\Gamma_3$	$\psi_2$	1	0	0	1	0	0	0
		2	0	0	-1	0	0	0
$\Gamma_9$	$\psi_3$	1	$\frac{1}{2}$	0	0	0	0	0
		2	$\frac{1}{2}$	0	0	0	0	0
	$\psi_4$	1	0	$\frac{1}{2}$	0	0	0	0
		2	0	$\frac{1}{2}$	0	0	0	0
$\Gamma_{10}$	$\psi_5$	1	0	$\frac{1}{2}$	0	0	0	0
		2	0	$-\frac{1}{2}$	0	0	0	0
	$\psi_6$	1	$-\frac{1}{2}$	0	0	0	0	0
		2	$\frac{1}{2}$	0	0	0	0	0

nonconventional superconductor compounds  $\text{PuCoGa}_5$  and  $\text{CeCoIn}_5$  and in particular to the higher superconductor critical temperature of the Ga-based compound.

#### ACKNOWLEDGMENTS

This work was supported by FAPESP (Grants 2008/11527-1, 2009/0947-3, 2009/10264-0, 2012/04870-7, 2012/10675-2), CNPq, and CAPES-Brazil. The authors thank the XRD2-LNLS staff for technical support and the LNLS for the beam time (proposals 8808, 10069, and 11045).

#### APPENDIX: MAGNETIC REPRESENTATION

The magnetic representation,  $\Gamma_{\text{Mag}}$ , of the rare earth site can be decomposed in terms of the four nonzero IR's ( $\Gamma_2$ ,  $\Gamma_3$ ,  $\Gamma_9$ , and  $\Gamma_{10}$ ) and their six basis vectors (BV's- $\psi_{1-6}$ ) associated with the Space Group  $P4/mmm$  (No. 123). The

IR's and the BV's are shown in Table III. The labeling of the propagation vector and the IR's follows the Kovalev's notation [30]. The IR's  $\Gamma_2$  and  $\Gamma_9$  correspond to a magnetic coupling where the magnetic unit cell is doubled in the  $c$  direction with a ferromagnetic coupling of the rare earth ions in each chemical unit cell forming a (+ + - -) sequence (model I). On the other hand, the IR's  $\Gamma_3$  and  $\Gamma_{10}$  correspond to a magnetic coupling where the two rare earth ions within the unit cell have an AFM coupling forming a (+ - - +) sequence (model II). In addition, the  $\Gamma_2$  and  $\Gamma_3$  represent the magnetic moment parallel to the  $c$  axis and  $\Gamma_9$  and  $\Gamma_{10}$  in the  $ab$  plane. The magnetic representation for the  $R_2\text{CoGa}_8$  series are summarized in Table III.

Comparing the experimental data and the simulated intensities, we can conclude that the magnetic structure for the  $\text{Gd}_2\text{CoGa}_8$  compound can be represented by the irreducible representation  $\Gamma_{10}$  and for both the  $\text{Tb}_2\text{CoGa}_8$  and  $\text{Dy}_2\text{CoGa}_8$  compounds, the magnetic representation can be better represented by  $\Gamma_2$ .

- 
- [1] J. Thompson and Z. Fisk, *J. Phys. Soc. Jpn.* **81**, 011002 (2012).
- [2] R. Movshovich, M. Jaime, J. D. Thompson, C. Petrovic, Z. Fisk, P. G. Pagliuso, and J. L. Sarrao, *Phys. Rev. Lett.* **86**, 5152 (2001).
- [3] J. Sarrao, L. Morales, J. Thompson, B. Scott, G. Stewart, F. Wastin, J. Rebizant, P. Boulet, E. Colineau, and G. Lander, *Nature (London)* **420**, 297 (2002).
- [4] N. J. Curro, J. L. Sarrao, J. D. Thompson, P. G. Pagliuso, S. Kos, Ar. Abanov, and D. Pines, *Phys. Rev. Lett.* **90**, 227202 (2003).
- [5] H. Hegger, C. Petrovic, E. G. Moshopoulou, M. F. Hundley, J. L. Sarrao, Z. Fisk, and J. D. Thompson, *Phys. Rev. Lett.* **84**, 4986 (2000).
- [6] J. Thompson, R. Movshovich, Z. Fisk, F. Bouquet, N. Curro, R. Fisher, P. Hammel, H. Hegger, M. Hundley, and M. Jaime, *J. Magn. Magn. Mater.* **226–230**, 5 (2001).
- [7] P. Pagliuso, D. Garcia, E. Miranda, E. Granado, R. Serrano, C. Giles, J. Duque, R. Urbano, C. Rettori, J. Thompson *et al.*, *J. Appl. Phys.* **99**, 08P703 (2006).
- [8] R. Lora-Serrano, C. Giles, E. Granado, D. J. Garcia, E. Miranda, O. Agüero, L. Mendonça Ferreira, J. G. S. Duque, and P. G. Pagliuso, *Phys. Rev. B* **74**, 214404 (2006).
- [9] C. Adriano, R. Lora-Serrano, C. Giles, F. de Bergevin, J. C. Lang, G. Srajer, C. Mazzoli, L. Paolasini, and P. G. Pagliuso, *Phys. Rev. B* **76**, 104515 (2007).
- [10] P. G. Pagliuso, J. D. Thompson, M. F. Hundley, J. L. Sarrao, and Z. Fisk, *Phys. Rev. B* **63**, 054426 (2001).
- [11] P. G. Pagliuso, J. D. Thompson, M. F. Hundley, and J. L. Sarrao, *Phys. Rev. B* **62**, 12266 (2000).
- [12] Wei Bao, P. G. Pagliuso, J. L. Sarrao, J. D. Thompson, Z. Fisk, and J. W. Lynn, *Phys. Rev. B* **64**, 020401(R) (2001).
- [13] E. Granado, P. G. Pagliuso, C. Giles, R. Lora-Serrano, F. Yokaichiya, and J. L. Sarrao, *Phys. Rev. B* **69**, 144411 (2004).
- [14] C. Adriano, C. Giles, L. Coelho, G. Faria, and P. Pagliuso, *Physica B* **404**, 3289 (2009).
- [15] C. Adriano, N. Aliouane, J. R. L. Mardegan, L. N. Coelho, R. Vescovi, P. G. Pagliuso, and C. Giles (unpublished).
- [16] R. D. Johnson, T. Frawley, P. Manuel, D. D. Khalyavin, C. Adriano, C. Giles, P. G. Pagliuso, and P. D. Hatton, *Phys. Rev. B* **82**, 104407 (2010).
- [17] Z. Fisk and J. Remeika, in *Handbook on the Physics and Chemistry of Rare Earths*, edited by K.A. Gschneider and L. Eyring, Vol. 12 (Elsevier, Amsterdam, 1989), p. 53.
- [18] D. A. Joshi, R. Nagalakshmi, S. K. Dhar, and A. Thamizhavel, *Phys. Rev. B* **77**, 174420 (2008).
- [19] C. Giles, F. Yokaichiya, S. Kycia, L. Sampaio, D. Ardiles-Saravia, M. Franco, and R. Neuenschwander, *J. Synchrotron Rad.* **10**, 430 (2003).
- [20] F. Vaillant, *Acta Cryst. A* **33**, 967 (1977).
- [21] J. Hill and D. McMorro, *Acta Cryst. A* **52**, 236 (1996).
- [22] Y. Joly, *Phys. Rev. B* **63**, 125120 (2001).
- [23] D. Gibbs, G. Grubel, D. R. Harshman, E. D. Isaacs, D. B. McWhan, D. Mills, and C. Vettier, *Phys. Rev. B* **43**, 5663 (1991).
- [24] M. F. Collins, *Magnetic Critical Scattering* (Oxford University Press, Oxford, 1989).
- [25] A. Wills, *Physica B* **276–278**, 680 (2000).
- [26] C. Detlefs, A. H. M. Z. Islam, A. I. Goldman, C. Stassis, P. C. Canfield, J. P. Hill, and D. Gibbs, *Phys. Rev. B* **55**, R680 (1997).
- [27] S. Nandi, Y. Su, Y. Xiao, S. Price, X. F. Wang, X. H. Chen, J. Herrero-Martín, C. Mazzoli, H. C. Walker, L. Paolasini, S. Francoual, D. K. Shukla, J. Stremper, T. Chatterji, C. M. N. Kumar, R. Mittal, H. M. Rønnow, Ch. Rüegg, D. F. McMorro, and Th. Brückel, *Phys. Rev. B* **84**, 054419 (2011).
- [28] S. Blundell, *Magnetism in Condensed Matter*, Oxford Master Series in Condensed Matter Physics (Oxford University Press, Oxford, 2001).
- [29] The density of states at the Fermi level for  $\text{Gd}_2\text{IrIn}_8$  was estimated using the electronic contribution to the heat capacity  $\gamma$  measured for the isomorphous reference compound  $\text{La}_2\text{IrIn}_8$ .
- [30] O. V. Kovalev, *Representations of the Crystallographic Space Groups*, 2nd ed., edited by H. T. Stokes and D. M. Hatch (Gordon and Breach Science Publishers, Yverdon, Switzerland, 1993).